Open Access

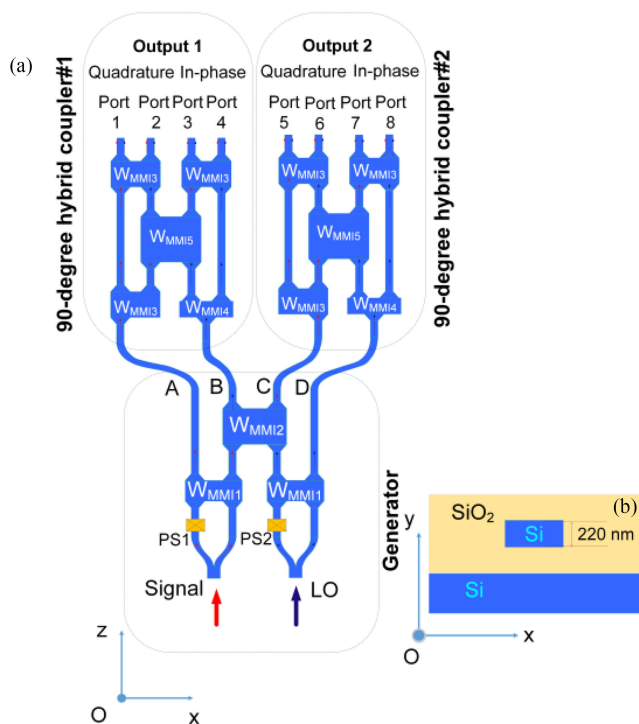# 1 × 2 Switchable Dual-Mode Optical 90° Hybrid Device Based on Thermo-Optic Phase Shifters and 2 × 2 MMI Couplers on SOI Platform

Duy Hai Ta
Hang Duy Nguyen Thi
Thanh Thuy Tran Thi
Khoi Nguyen Do Hoang
Van Cuong Chu
Trung Hieu Nguyen
Cao Dung Truong

1 × 2 Switchable Dual-Mode Optical 90° Hybrid Device Based on Thermo-Optic Phase Shifters and 2 × 2 MMI Couplers on SOI Platform

**Duy Hai Ta, Hang Duy Nguyen Thi, Thanh Thuy Tran Thi,
Khoi Nguyen Do Hoang, Van Cuong Chu, Trung Hieu Nguyen,
and Cao Dung Truong** [ORCID]

Faculty of Electronic Engineering, Posts and Telecommunications Institute of Technology,
Hanoi 150000, Vietnam

Abstract: This paper designs a 1 × 2 switchable dual-mode optical 90° hybrid device on the silicon-on-insulator (SOI) platform for the mode division multiplexing hybridized coherent transmission systems in optical communication. Our proposed hybrid uses various 2 × 2 multimode interference (MMI) couplers, symmetric Y-junctions, and thermo-optic phase shifters. The suggested hybrid device working principle is proved on theoretical analysis about the multimode interference and the transfer matrix relation. The optimization of geometrical parameters and metallic micro-heaters is executed through the numerical simulation method. The proposed hybrid coupler expresses lots of optical performance advantages, with an insertion loss lower than 2.5 dB, a common-mode rejection ratio (CMRR) better than −24 dB, and phase error smaller than 4° in the 50-nm wavelength bandwidth of the third telecom window for both two TE modes. Besides, the device is proven large geometrical tolerances in terms of width and height tolerances larger than ±50 nm and ±6 nm in the 1.5-dB variation limit of transmission, respectively. In addition, the proposed device attains relatively low power consumption under 75 mW and an ultrafast switching time below 10 μs. Such advantages of good performances make the device a promising potential for broadband and intra-chip MDM-hybridized coherent optical communication systems and photonic integrated circuits.

Index Terms: Switchable, 90° optical hybrid coupler, mode division multiplexing, thermo-optic phase shifters, numeric simulation, silicon-on-insulator (SOI).

1. Introduction

Today, one of the leading solutions widely applied in optical transmission systems is the coherent transmission technique. Coherent transmission systems are often incorporative into some advanced modulation techniques such as quadrature amplitude modulation (QAM) [1]–[3] and quadrature phase-shift keying (QPSK) modulation for carrying high bitrate in optical transmission

systems [4]. Such systems have been deployed in long-haul transmission systems to enhance the spectral efficiency and transmission capacity of the next-generation networks. They must suffer a hefty traffic load from wide-area information networks. Compared to other traditional transmission systems, i.e., wavelength division multiplexing (WDM) systems, coherent transmission systems considerably prevail in significant spectral efficiency and high sensitivity and high tolerance to amplified spontaneous emission (ASE) noise thanks to digital signal processing processes (DSP) at both the transmitter and receiver. Also, the coherent optical transmission technique achieves better qualities for both chromatic dispersion (CD) and polarization mode dispersion (PMD) because of the negligible impact of the wavelength-dependent refractive index effect. Moreover, coherent optical transmission systems also offer higher bitrates, greater flexibility, simpler photonic systems, and better optical performance with more advanced modulation techniques in the next-generation optical communication systems.

Optical hybrid couplers play the most prerequisite component in a coherent transmission system, enabling hybridization in the complex-vector space between the phase-modulated signal and multilevel-modulated signals, including amplitude-phase in the mixture with the reference signal originated from a local oscillator (LO). The hybridized signals are lead to the arrayed balanced detectors for the receiving and signal processing components. Such the receiver is capable of detecting advanced phase-modulated and amplitude-modulated signals. According to various applied purposes in optical communication systems, there are several forms of optical hybrid couplers have been introduced and demonstrated in practice, such as 72° hybrid coupler for multilevel modulation schemes [5], 120° hybrid coupler for polarization-division-multiplexed quadrature phase-shift keying signals or pulse amplitude modulation schemes [6]–[8], and 180° hybrid coupler for M-ary quadrature amplitude modulation (M-QAM) schemes [9]. Among different kinds of optical hybrid couplers, the optical 90° hybrid coupler may be one of the most popular optical hybrid coupler to detect the optical signal divided into in-phase and quadrature-phase planes, such as the quadrature phase-shift keying (QPSK) signal. Currently, the 90° hybrid coupler is now being widely applied in a variety of communication systems, for instance, microwave communication [10], radio over fiber system [11], [12], optical fiber communication [13]. Several kinds of the 90° hybrid device based on optical waveguides have been investigated and demonstrated on various structures, such as Mach-Zehnder interferometers [13], star couplers [14], Bragg gratings [15], [16], arrayed waveguide gratings (AWG) [17], multimode interference (MMI) couplers [18], photonic crystals [19] or plasmonic waveguides [20]. MMI coupler-based hybrids are preferred to recognize an on-chip integrated photonic device thanks to flexible configurations and significant fabrication tolerances [21], [22]. Hence, plenty of material platforms are introduced for MMI couplers-based optical hybrids including InP [23]–[25], LiNbO$_3$ [26] and silicon-on-insulator (SOI) [27]–[30], silicon nitride (Si$_3$N$_4$) [31]. Recently, SOI-based waveguides have become a favorite choice for photonic devices due to their remarkable properties of high confinement of light, low-bending loss, compatibility to the complementary metal-oxide-semiconductor (CMOS) technology.Thus, they lead to the reasonable manufacturing cost [32].

Besides, to date, the mode division multiplexing technique is also an up-and-coming solution to increase optical channel capacity, especially in MDM-hybridized WDM systems [33], [34]. Because, in the MDM system, each spatial orthogonal guided wave mode behaves as a wavelength-independent channel. Therefore, the MDM technique is especially preferable in on-chip photonic communication and computation systems. Many functional components based on the SOI material platform have been reported in numerous investigations, such as mode demultiplexer [35], [36], and mode switch [37]–[39]. However, there is a significant lack of research on hybrid systems between MDM and coherent optical communication. Optical 90° hybrid devices are typically designed in a fixed configuration for only a specific wavelength range without supporting the switching function [40]. Roland Ryf *et al.* [41] have experimentally demonstrated a six-mode optical fiber communication system with a long-distance propagation up to 96 km using coherent 6 × 6 MIMO processing technique since 2012. A coherent few-mode multiplexer has recently been experimentally constructed to coupe eight modes in a few-mode fiber (FMF) with a silicon photonic chip allowing processing a total capacity of eight coherent optical channels [42].
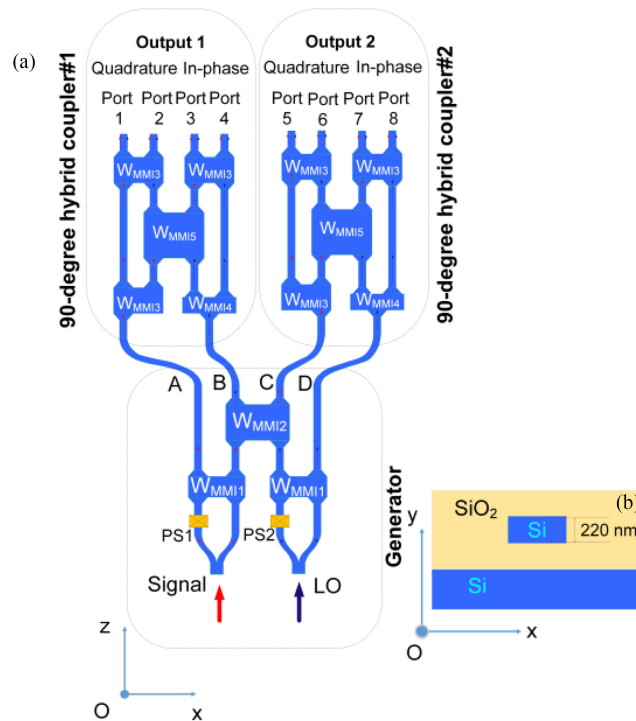
Fig. 1. Sketch diagram of the 1 × 2 switchable dual-mode silicon 90-degree optical hybrid coupler based on the SOI channel waveguide driven by two controllable phase shifters: (a) side view, and (b) cross view.

This paper proposes a 1 × 2 switchable dual-mode optical 90° hybrid device based on the SOI platform enabling the MDM-hybridized coherent transmission system. First, the device can operate in a 1:1 mono-mode optical 90° hybrid coupler protection configuration for each guided mode. Second, the device can operate as an exchangeable two-mode division demultiplexed optical 90° coupler for two simultaneous modes. The switching states can be controlled under the impact of the thermo-optic effect via the utilization of metallic heaters.

2. Working Principle and Optimization

A 1 × 2 switchable dual-mode silicon optical 90° (90-degree) hybrid device is constituted from two major fundamental elements, including a mixture signal generator and two optical 90-degree hybrid couplers, as shown in Fig. 1. The former is a dual-mode hybrid switching mechanism between two input signals comprising a local oscillator (LO) signal and a phase-modulated information signal, briefly denoted as Signal. In contrast, the latter plays the role of a coherent receiver. The proposed device is designed to support the propagation of two waveguide modes of the transverse electric (TE) polarization state in the third telecom window with the central wavelength $\lambda = 1550$ nm. The structure is constructed on the silicon-on-insulator material platform. Herein, the core layer is made from the silicon (Si) crystal and is structured in the channel waveguide form with the 220-nm thickness entirely covered by the silica layer (SiO$_2$). Both input waveguides support the two lowest modes of TE$_0$ and TE$_1$, and therefore, the width of input waveguides W_0 is initially set up as 0.9 μm.

Based on two of these mentioned components, the MMI coupler becomes more vital. The explanation is because the relationship between the amplitude and the phase angle are adaptively configured. The phase relations between the inputs and outputs of the MMI coupler depend on the placed locations and the multimode region length of L_{MMI} due to the specific property following the self-imaging theory when compared to the half-beat length of L_π. According to the

self-imaging principle, L_π is defined as the beat length between two lowest-order modes, which can be calculated as:

$$L_\pi = \frac{4n_e W_e^2}{3\lambda} \tag{1}$$

In which $W_e = W_{MMI} + \frac{\pi}{\lambda}(n_e^2 - n_c^2)^{-1/2}$ for TE polarization mode; where λ is the operating wavelength; n_e is the effective refractive index of the silicon core layer; n_c is the refractive index of the cladding layer; W_{MMI} and W_e correspond the geometrical width and the effective width of the MMI coupler, respectively. For each MMI coupler, the selected length of L_{MMI} depends on the interference images needing to be reformed. We use five different kinds of 2 × 2 MMI couplers belonging to the general interference (GI) mechanism in this proposed design, as denoted in Fig. 1(a). These couplers are utilized to realize the function of a two-mode mixture signal generator and a coherent optical 90-degree hybrid coupler.

The two-mode mixture signal generator, briefly so-called the generator, is designed for simultaneously switching the LO signal and the phase-modulated information signal (Signal) in the switching configuration of the 1 × 2 switch for two guided modes of TE_0 and TE_1. This element includes two dual-mode demultiplexers to carry out the demultiplexing mission for dedicated inputs of Signal and LO. This element also uses a crossover coupler (X-coupler) by using a 2 × 2 multimode interference coupler (MMI2) to be a bridge across dual branches in the switchable configuration. The two-mode demultiplexer composes an asymmetric Y-junction coupler, a 2 × 2 multimode interference coupler (MMI1) playing as a 3-dB coupler (50:50 power splitter), and a controllable phase shifter as sketched in Fig. 1(a). It is well-known that the symmetric Y-junction operates as a 3-dB mode-order divider, in which the fundamental mode of TE_0 at the stem is split into two in-phase fundamental modes in two access arms at the output. In contrast, the first-order mode of TE_1 at the stem is split into two counter-phase fundamental modes. Two sinusoidal waveguides separate the Y-junction at two output branches with a reasonable bending radius to achieve a negligible bending loss and an acceptable size. In this design, the sinusoidal waveguide has a gap G in the horizontal direction of the x-coordinate and a length L_S in the propagation direction of the z-coordinate. Before connecting to the MMI1 coupler, we place a controllable phase shifter with a suitable phase-shift to perform a mode division demultiplexing function by combing the optical fields from two access arms. The MMI1 coupler in this design has the length $L_{MMI1}3 = L_\pi/2$ whose the transfer matrix is defined by:

$$M_1 = \frac{1}{\sqrt{2}} \begin{pmatrix} 1 & j \\ j & 1 \end{pmatrix} \tag{2}$$

Therefore, if the phase shifter has the phase difference $\Delta\Phi = \pm\pi/2$, the MMI1 coupler will separate two order modes from the stem input into two individual fundamental modes at the outputs of the MMI1 coupler.

Hardly can this device realize the mixture function of LO and the Signal without two 90° hybrid couplers. Therefore, the device needs two 90° hybrid couplers so that each hybrid coupler is mainly constructed from three various kinds of 2 ×2 MMI couplers, as presented in Fig. 1(a). First, the 1 × 2 MMI3 coupler with the length of $L_{MMI3}3 = L_\pi/2$ is placed on the left to connect to the Signal port. Second, the symmetric 1 × 2 MMI4 coupler with the length of $L_{MMI4}3 = L_\pi/8$ is put on the right side to connect to the LO port. On the top of Fig. 2(a), we place two 2 × 2 MMI3 couplers with the length $L_{MMI3}3 = L_\pi/2$ playing roles of 3-dB couplers. Finally, the 2 × 2 MMI5 coupler is put in the middle section to be responsible for a bridge over two individual branches. Therefore, the MMI5 coupler length should be installed as $L_{MMI5}3 = L_\pi$ because the mirrored-imaging effect will be reproduced if the multimode region length is equal to three times the half-beat length L_π [43]. Transfer matrices of different MMI couplers mentioned are calculated by following the interference theory [44]:
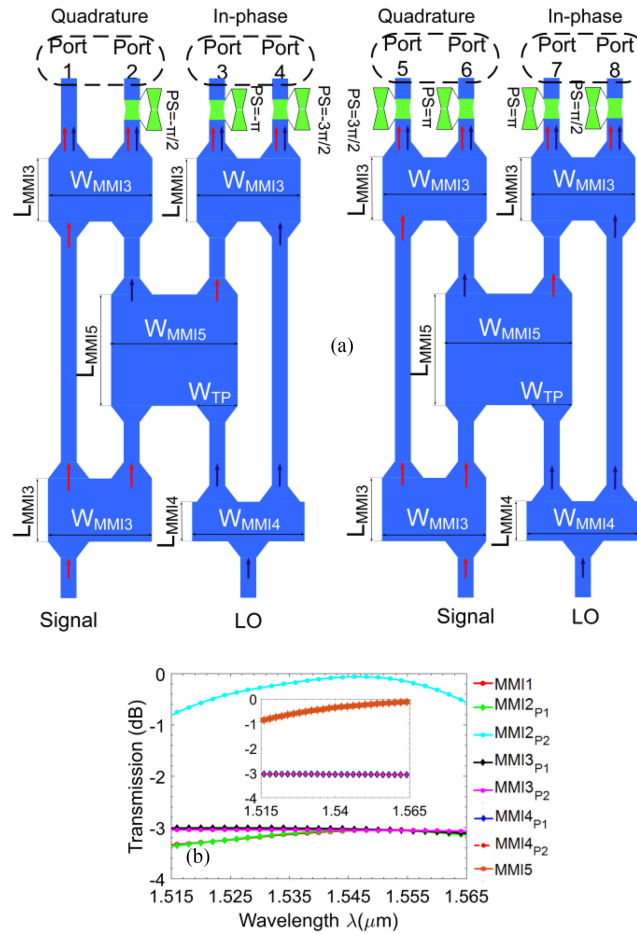
Fig. 2. (a) Working diagram of the optical hybrid coupler based on 2 × 2 MMI couplers. (b) Transmission characteristics of five kinds of MMI couplers on the wavelength response in the third telecom windows.

$$M_3 = \frac{1}{\sqrt{2}} \begin{pmatrix} 1 & j \\ j & 1 \end{pmatrix} \text{ for } L_{MMI3} = 3L_\pi/2$$

$$M_4 = \frac{1}{\sqrt{2}} \begin{pmatrix} e^{j\pi/2} \\ e^{j\pi/2} \end{pmatrix} \text{ for } L_{MMI4} = 3L_\pi/8$$

$$M_5 = \begin{pmatrix} 0 & j \\ j & 0 \end{pmatrix} \text{ for } L_{MMI5} = 3L_\pi \tag{3}$$

We suppose that the total optical energy is not attenuated when passing through MMI couplers, and the phase is attained in the ideal condition. From Exp. (1–3), we obtain the expressions for four output ports of the coherent receiver as:

$$\begin{pmatrix} E_1 \\ E_2 \\ E_3 \\ E_4 \end{pmatrix} = \begin{pmatrix} S - jL \\ j(S + jL) \\ -(S + L) \\ -j(S - L) \end{pmatrix} \tag{4}$$

where S and L indicate the amplitude of Signal and LO, respectively; E_1, E_2, E_3, and E_4 denote the complex amplitudes of electric fields at the output ports of the 90° hybrid coupler.

90-degree hybrid coupler#1

| Signal LO | Signal LO | Signal LO | Signal LO |
| ΔΘ=0 | ΔΘ=π/2 | ΔΘ=π | ΔΘ=-π/2 |

90-degree hybrid coupler#2

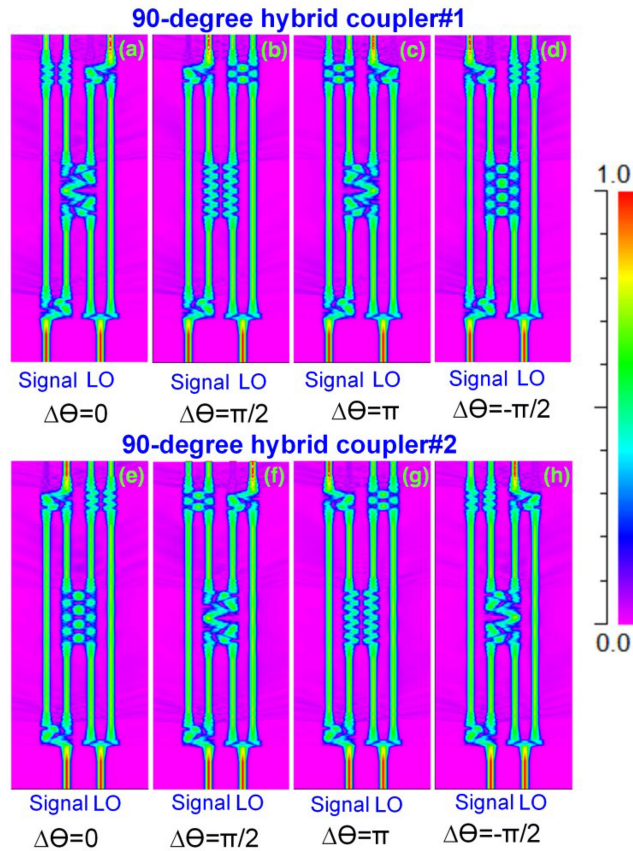| Signal LO | Signal LO | Signal LO | Signal LO |
| ΔΘ=0 | ΔΘ=π/2 | ΔΘ=π | ΔΘ=-π/2 |

Fig. 3. Simulated electromagnetic field distributions for two designed 90-degree hybrid couplers. (a-d) for the first hybrid coupler, and (e-h) for the second hybrid coupler, respectively. The amplitude is identical for Signal and LO.

By adjusting the phase angle at the outputs of the 90° hybrid coupler to achieve a pair of in-phase and quadrature complicated signals, we need to use three additionally fixed phase shifters behind the outputs with phase differences corresponding to $-\pi/2$, $-\pi$, and $-3\pi/2$ (shown as Fig), respectively. Besides, the optical attenuation is non-excludable, and therefore, the real transfer matrix relationship of complex amplitudes can be rewritten as follows:

$$\begin{pmatrix} E'_1 \\ E'_2 \\ E'_3 \\ E'_4 \end{pmatrix} = \begin{pmatrix} \kappa_1 (S - jL) \\ \kappa_2 (S + jL) \\ \kappa_3 (S + L) \\ \kappa_4 (S - L) \end{pmatrix} \tag{5}$$

where κ_1, κ_2, κ_3, and κ_4 are corresponding to transmission coefficients of four ports at the output of the 90° hybrid; E'_1, E'_2, E'_3, and E'_4 are realistically complex amplitudes of distributed electric field patterns at four output ports of the suggested device. (5) shows that the proposed structures are shown in Fig. 2(a) act as 90-deg hybrid optical couplers because of the complicated amplitude relationship at the outputs, in each, a set of four outputs is reformed by a couple of in-phase or quadrature. Note that, to realize the same result for the second 90° hybrid coupler when compared to the first 90° hybrid coupler, we insert four fixed phase shifters with phase differences corresponding to $3\pi/2$, π, π, and $\pi/2$, respectively.

Fig. 3 shows the simulated electromagnetic field patterns of two optimally designed 90-degree optical hybrid couplers in the appearance of Signal and LO with four-phase difference (ΔΦ) states. As can be seen in subfigures of Fig. 3, when $\Delta\Phi = 0$ (rad) or π (rad), output intensity ratios for

TABLE 1
Waveguide Geometric Dimension

Symbol	Value	Symbol	Value
W_{MMI1}	3.8 μm	L_{MMI4}	9 μm
W_{MMI2}	3.8 μm	L_{MMI5}	65 μm
W_{MMI3}	2.6 μm	WPS	2 μm
W_{MMI4}	3 μm	L_{PS}	300 μm
W_{MMI5}	2.9 μm	H_{PS}	0.1 μm
L_{MMI1}	56.8 μm	W_0	0.9 μm
L_{MMI2}	114 μm	L_S	130 μm
L_{MMI3}	28 μm	G	1.4 μm

each output channels are 0.5:0.5:0:1 and 0.5:0.5:1:0, respectively. Besides, output intensity ratios for the first one and the second one of 90-degree hybrid couplers are 0.5:0.5:0:1 and 0:1:0.5:0.5, respectively. This evidence corresponds to the working principle described in (5). Similar observations from Fig. 3 also demonstrate that the operation of optical fields is the accordance with the theoretical analysis for both two proposed optical hybrid couplers.

For a material platform with a high contrast of refractive indices like SOI, an efficiently rigorous numerical simulation method based on the three-dimensional finite-difference techniques is applied to simulate and optimize the suggested device with efficient grid sizes $\Delta x = \Delta y = \Delta z = 5$ nm. The geometrical parameters in this design optimized by using numerical simulations are listed on Table 1. Fig. 2(a) shows the conceptual diagram of two 90° hybrid couplers consisting of various 2 × 2 MMI couplers, and Fig. 2(b) exhibits all transmission curves of the suggested MMI couplers on the dependence of wavelength response in the range 1515-1565 nm. As can be seen, 3-dB MMI couplers are nearly perfect because of negligible optical loss with a flat wavelength response in a continuum wavelength band. Meanwhile, crossover MMI couplers are relatively low-loss with variation loss smaller than 1-dB in broadband of 50-nm and optimal at the central wavelength of 1550 nm. Besides, to improve the coupling efficiency, linear tapers are located to connect between single-mode access waveguides and multimode interference regions. Using the numerical simulation process, we find out geometrical parameters of the applied linear tapers corresponding to their width and length as $W_{TP} = 1$ μm and $L_{TP} = 20$ μm, respectively.

Two controllable phase shifters play a pivotal role in realizing the switching states for the proposed device. In this paper, controllable phase shifters are thermo-optic phase shifters using the thermo-optic effect to control the phase angle of optical fields when propagating through metallic microheaters. Micro heaters are constructed from a metallic Ti/W thin film whose thickness of H_{PS}, longitude length of L_{PS}, and horizontal width W_{PS} deposited on the top above the silicon waveguide by a gap of $h_{SiO2} = 700$ nm [45]. The function of the generator is switching and exchanging mode. The higher-order mode is exchanged to the fundamental mode when passing through the symmetric Y-junction and the MMI1 coupler under the controllable phase shifter impact while the fundamental mode attains the order. An outer port of each MMI1 connects to the MMI2 coupler for crossing the optical signal. With this designed generator, Signal and LO are switched to the right side or the left side to take a pair. The phase shifter is controlled by heating the waveguide from a thermal source to reach the critical phase difference of $\pm\pi/2$. The relationship between phase and index change under the influence of the thermo-optic effect is determined by the following formula
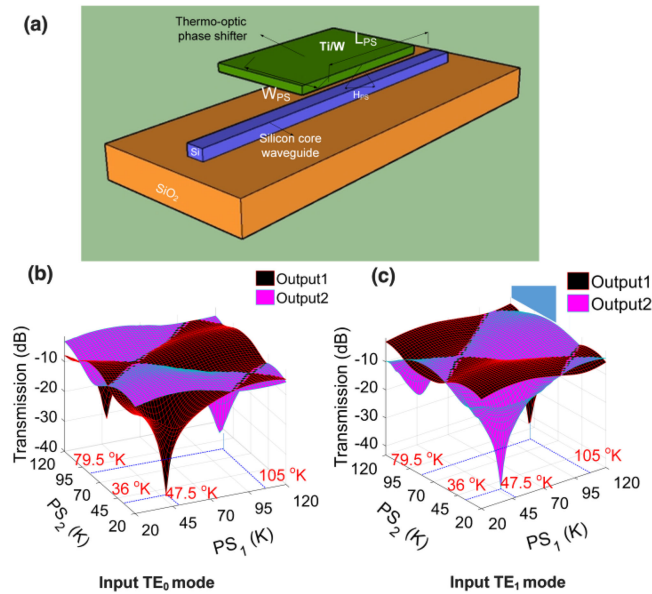
Fig. 4. Structure and operation of the controllable phase shifters based on the metallic micro-heater: (a) sketched diagram, (b) transmission response at outputs of the generator for TE_0 mode, and (c) transmission response at outputs of the generator for TE_0 mode.

[46]:

$$\Delta\Phi = k\Delta n L_{PS} \tag{6}$$

where L_{PS} is the heater length in the propagation direction and $k = 2\pi/\lambda$ is the wavelength number; Δn is the index changed determined in the relation with the thermal coefficient, dn/dT, and can be calculated as:

$$\Delta n = \frac{dn}{dT}\Delta T \tag{7}$$

Here, the thermal coefficient for silicon is $dn/dT = 1.84 \times 10^{-4}$ K^{-1} at room temperature. Fig. 4(a) shows the general sketched diagram of two controllable phase shifters. Initially, we choose dn/dT suitably geometrical parameters of the thermo-optic phase shifters (TOPS) as $L_{PS} = 300$ μm, $W_{PS} = 2$ μm, and heater-thickness $H_{PS} = 100$ nm. Two TO phase shifter, PS1, and PS2, are used for tuning required phases to implement reconfigurable switching and exchanging modes. By injecting the optical fields into input ports of Signal and LO for two modes of TE polarization states, transmission responses at each output ports of the generator, measured by numerical simulation data, are investigated as a bivariable function of temperature changes ΔT_1, ΔT_2 corresponding to controllable phase shifters PS1 and PS2. Results plotted in Fig. 4(b,c) show that the transmission at the Output1 (the left branch of output ports of the MM1 coupler) is maximal when $(\Delta T_1, \Delta T_2) = (47.5$ °K, 36 °K) and minimal when $(\Delta T_1, \Delta T_2) = (105$ °K, 79.5 °K) if the input mode is TE_0 and vice versa if the input mode is TE_1. This case is the switching state "OFF". Results are contrary in the situation at the Output2 (the right branch of output ports of the MMI1 coupler), corresponding to the switching state "ON". All waveguide geometric parameters that are selected or optimized by simulation are listed on Table 1.

3. Device Characterization and Discussion

To investigate and evaluate optical performances of the proposed switchable silicon optical 90° hybrid coupler, we apply the 3D-beam propagation method based on the finite-difference technique as a rigorous and reliant method to simulate the working evolution, performance optimization, and
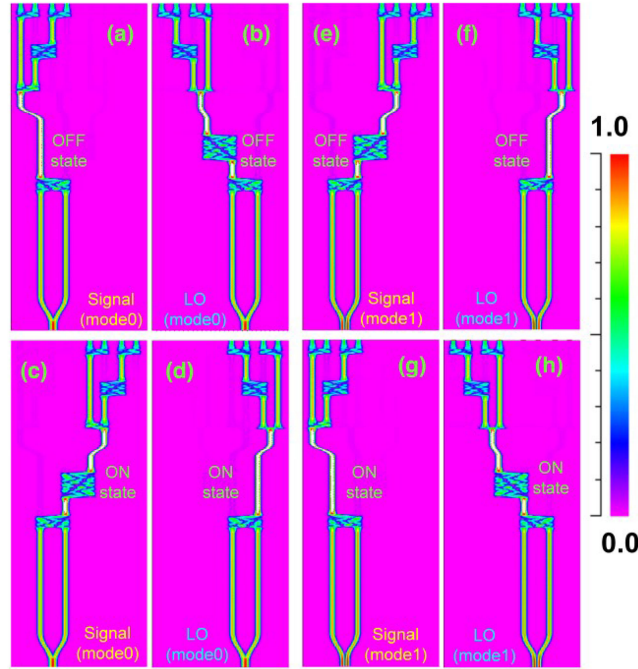
Fig. 5. Propagation field distributions of the Poynting vector for the proposed device under the control of two thermo-optic phase shifters at two switching states of "OFF" and "ON" for two TE modes correspondingly shown to subfigures from (a) to (h), respectively.

characterization of the device. The propagation field distributions of the Poynting vector under the control of two thermo-optic phase shifters at two switching states of "ON" and "OFF" for two TE modes are calculated using the 3D-semivectorial BPM method and shown in Fig. 5. One can visually perceive that two lowest order TE modes from the Signal port and the LO port can be switched entirely and hybridized correctly to the corresponding output ports as analyzed by the theory. Also, simulated propagation fields prove that if only a unique guided mode of TE_0 or TE_1 is used for simultaneous generations of Signal and LO ports, the designed device will act as a 90° hybrid switch in the 1:1 protection configuration. If both of the two guided modes of TE_0 and TE_1 are injected, the proposed device will work as an exchangeable dual-mode 90° hybrid demultiplexer.

Some criteria parameters, including insertion loss, common-mode rejection ratio, imbalance factor, and phase error, have been investigated and characterized via numerical simulation methods. Those are critical optical characteristics on the aspect of the physical property to validate the optical performances of a hybrid optical device.

Insertion loss is defined as a subtraction between the output power of each output port and the input power in the decibel unit described by the following formula:

$$IL = 10log_{10}\left(\frac{P_i}{P_{in}}\right), i = \overline{1,8} \tag{8}$$

where P_{in} is the normalized input power by a unit, P_i is the desired power for each output port i-th.

The following formula calculates the common-mode rejection ratio:

$$CMRR_I = 20log_{10}\left(\left|\frac{P_{Ip}-P_{In}}{P_{Ip}+P_{In}}\right|\right) \tag{9}$$

$$CMRR_Q = 20log_{10}\left(\left|\frac{P_{Qp}-P_{Qn}}{P_{Qp}+P_{Qn}}\right|\right) \tag{10}$$
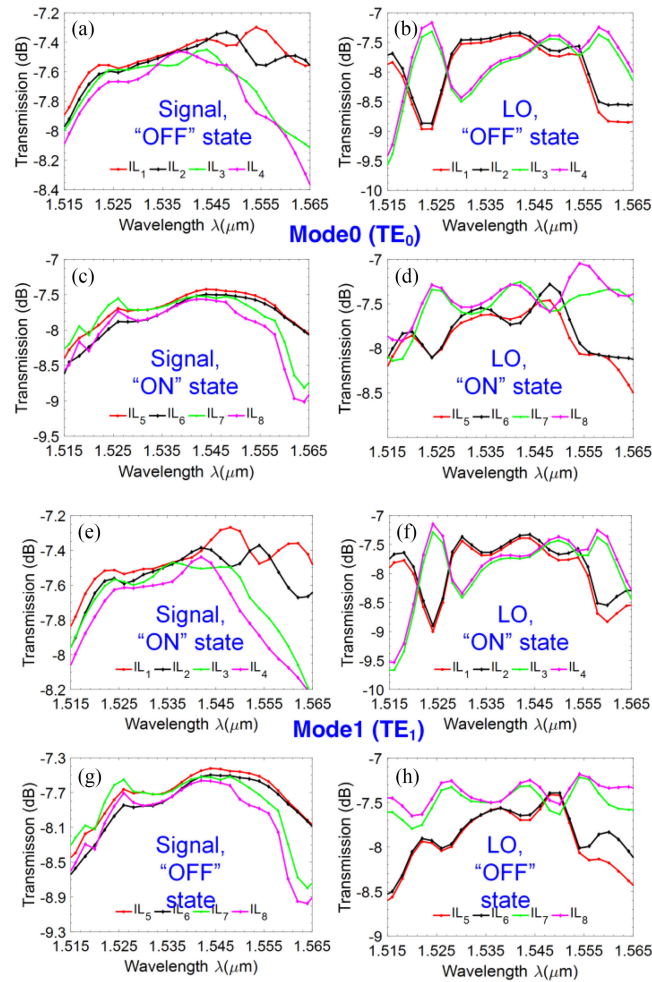
Fig. 6. Transmission response plots at the output ports of the device on the wavelength dependence for two modes of Signal and LO and two switching states corresponding to subfigures from (a) to (h), respectively.

Here, the quadrature and in-phase channels are represented as symbol "Q" and "I"; p and n symbolize the positive and negative signs before algebra expressions for the IQ channels, respectively.

Imbalance factor is defined as the power of the positive ports subtracted by the power from the negative ports as given in:

$$Imbalance_I = 10 log_{10} \left(\left| \frac{P_{Ip}}{P_{In}} \right| \right) \tag{11}$$

$$Imbalance_Q = 10 log_{10} \left(\left| \frac{P_{Qp}}{P_{Qn}} \right| \right) \tag{12}$$

Fig. 6(a)–(h) show the transmission properties of individual insertion loss of two modes for Signal and LO inputs dedicated to output ports, as wavelength-dependent functions corresponding to the different states from the presented figures of Fig. 6(a)–(h). The dedicated insertion loss level for each individually separated output port varies from −7.3 dB to −9.0 dB for the phase-modulated signal and −7 dB to −9.5 dB for the local oscillator signal in the wavelength range from 1515 nm to 1565 nm. Importantly noted that the optical signal at each input port is always divided into four output branches, as seen in Fig. 5(the splitting ratio of 4 is equivalent to the 6-dB attenuator).
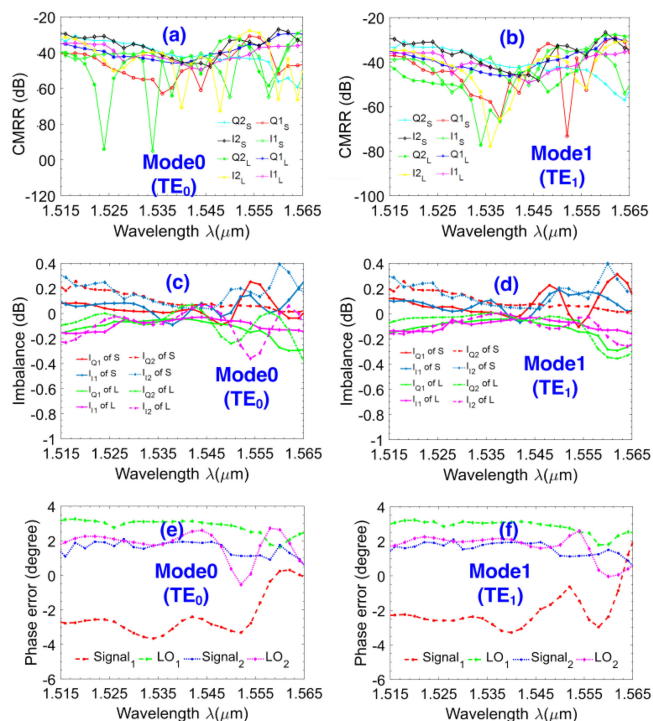
Fig. 7. Wavelength spectra of optical characteristic parameters for input ports of TE_0 and TE_1 corresponding to (a-b) CMRR, (c-d) imbalance factor, and (e-f) phase error, respectively.

Therefore, the total propagation loss of optical fields in the proposed device is relatively low-loss, not exceed 2.5 dB in 50-nm wavelength bandwidth for all cases. As a consequence, the 3-dB wavelength bandwidth of the designed device is more extensive than 50-nm.

Assume that *S* and *L* are brief symbols for the Signal port and the LO port in the IQ channels for two modes. We continually survey CMRR based on wavelength dependency that its behavior is an essential optical factor to estimate a distinguished level in the complex signal. The results of the wavelength-dependent CMRR are plotted in Fig. 7 (a, b) for TE_0 and TE_1 modes. The CMRR factor is less than −24 dB in the whole 50-nm bandwidth of the surveyed wavelength range. Besides, it is expected that the device operates as an excellent coherent optical receiver, the power balance between output ports of in-phase and quadrature channels should be negligibly small. Fig. 7(c, d) show the computed values of imbalance factors for both TE_0 and TE_1 modes. The imbalance factor of the output ports of TE_0 and TE_1 modes fluctuates relatively small variations from −0.4 dB to 0.4 dB for both TE_0 and TE_1 modes, over 50 nm of the C-band spectral range. A little change of studied imbalance factors is a critical characteristic for realizing good coherent optical receivers. In addition, in a digital signal processing process of the complicated signal like an advanced phase-modulated signal, the phase error may cause a considerable error on balanced photodiodes and detectors. As presented in Fig. 7(e,f), the phase deviations over the surveyed 50-nm wavelength band of the 1550 nm windows are less than $|4^o|$ for both two modes.

In order to recognize the correctness between theoretical analysis in the equation system of (5) and the numerical simulation, we investigate the dependence of transmission characteristics of optical power and phase angle of the output ports on the wavelength when separately transmitting the phase-modulated carrier and the LO signal into the corresponding input ports of the TE_0 mode. Simulation data for the phase diagrams of IQ channels is plotted in the polar coordinate system, as shown in Fig. 8. Herein, the radius coordinate presents the transmission of output ports, while the phase angle coordinate shows the phase value corresponding to each value of optical power at output ports following the wavelength response. Fig. 8(a) shows simulation results
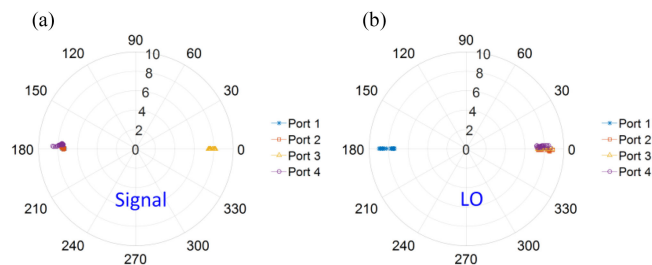
Fig. 8. Representation of amplitudes and phase angles of the TE$_0$ input on wavelength dependency in the polar coordinate system for (a) phase modulated signal and (b) LO.

for the information signal modulated by the phase-shift keying launched into the left input port. Fig. 8(b) exhibits simulation results for the LO signal injected into the right input port. It is visible to the amplitudes as well as phase angles of the complex signals shown in Fig. 8 are suitable to (5) for both I and Q channels. Intuitive images also exhibit a few deviations of the output powers (not exceeded ± 1 dB) and phase angles (not exceed 5°) at output ports in the wide range over 50-nm bandwidth, thus proving the device is broadband.

Additionally, the deviation of three-dimensional geometrical parameters has a considerable effect on optical performance in photonic integrated circuits. Most manufacturing processes of devices always exist an inaccuracy of tolerances due to the imperfect fabrication process or the undesirable SOI wafer quality. Besides, for the simulation-based design, the simulation model also plays an important role, such as computational algorithm, grid sizes of the simulation method contributing to the variation of tolerances. A waveguide width tolerance is investigated within $W_0 \pm \Delta w$, in which W_0 is the nominal width of the input waveguides as equal as 0.9 μm, and Δw is the deviation of the width caused by the manufacturing error. Fig. 9 shows the simulated insertion loss of dedicated output ports as functions of the width tolerance for two modes and two switching states. Results indicate that the total loss fluctuation is varied lower than 1-dB in the ±50-nm tolerance gap because variations only fluctuate about −7 dB to −8 dB. Also, Fig. 10 illustrates the height tolerances for IL of the device. The results depict that IL slightly fluctuates from −7.1 dB to −8.5 dB in the silicon waveguide height tolerance of $\Delta h = \pm 6$ nm (the height H of the silicon layer is equal to 220 nm), for all cases of guided modes and switching states.

Under the thermo-optic effect impact, the phase tuning process can attain by a voltage-driven metallic microheater. Furthermore, this mechanism can be utilized with a negligible optical loss by placing the metallic microheater at a determined distance on the top side of the core waveguide. However, the heater is typically located far from the waveguide by the micrometer scale, leading to low-performance levels on aspects of high power consumption or low switching speed. It is impressive that the shifted phase angle is not dependent on the heater length as well as the metallic material of the heater, L_{PS}, but depends a lot on the electric power consumption [47]. Hence, the induced phase shift is the same for a given power consumption regarding to the heater length. Naturally, in a TOPS, we expect to obtain the optimal product of $P_\pi . \tau = H . \Delta T_\pi$ during the switching operation process [45], [48]. Here, H stands for the heat capacity, ΔT_π is the changing temperature from a cold state to a hot state to attain the expected phase shift of π, and τ is the switching time relating to the phase shifter temporal response and the cut-off frequency $f_{cut\text{-}off}$ [49]. However, the descent of the power consumption P_π in the switching operation may cause a considerable quality of the switching time. Also, smaller power consumption should be kept at an acceptable level.

Because when the gap between the metallic heater and the silicon core h_{SiO_2} is small (see in Fig. 3(a)), the influence of the plasmonic effect on the lightwave propagation in terms of phase difference and optical loss becomes more significant. For instance, if h_{SiO_2} is small enough in several nanometers, the plasmonic effect will strongly hybridize photonic modes in the silicon core layer with plasmonic modes near the metal-dielectric interface. Therefore, this hybridization can lead to a high absorption loss for the photonic modes.
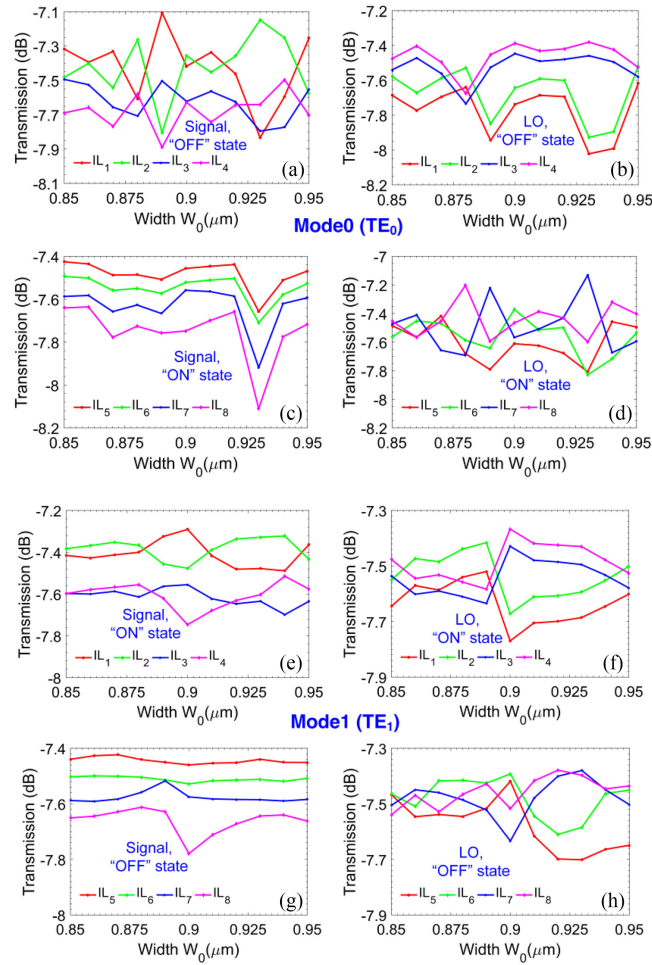
Fig. 9. Transmission properties at the output ports of the device as a function of the width tolerance for two modes of Signal and LO and two switching states: (a–d) for TE_0 mode, and (e–h) for TE_1 mode.

The switching consumption power is a specific parameter representing the electric power consumption efficiency in a photonic device which is based on the thermo-optic effect. This parameter can be determined by the utilization of a modified two-dimensional treatment of the heat flow on the lateral spreading as follows [50]:

$$P_\pi = \frac{\lambda \kappa_{SiO_2} \left(\frac{W_{PS}}{h_{SiO_2}} + 0.88 \right)}{\left| \frac{\partial n}{\partial T} \right|} \tag{13}$$

where $\kappa_{SiO_2} = 1.4$ W/(m.K) is the thermal conductivity of SiO_2, λ is the operation wavelength, and W_{PS} is the Ti-metal film width in the lateral direction. The switching time characterized by the TO phase shifter response time directly relates to the cut-off frequency by $\tau = \frac{1}{e.f_{cut-off}}$. In which the cut-off frequency directly relates to the switching power as follows [49]:

$$f_{cut-off} = \frac{P_\pi}{\pi \rho_{SiO_2} C_{SiO_2} A} \left| \frac{\partial n}{\partial T} \right| \tag{14}$$

where $\rho_{SiO_2} = 2.203$ g/cm³ is the density of silica, $C_{SiO_2} = 0.703$ J/(g.K) is specific heat capacity, and A denotes the effectively heated cross-section area relating to the geometry parameters of the TO phase shifter.
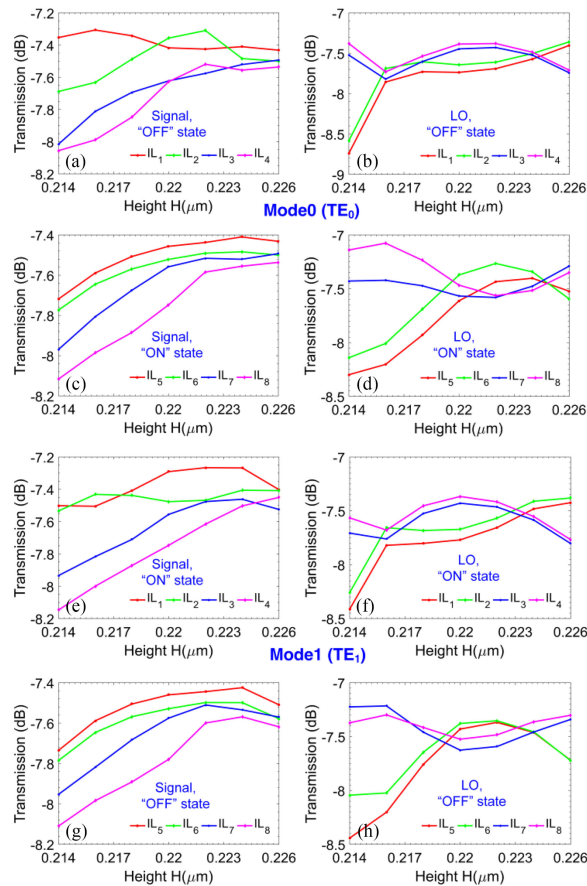
Fig. 10. Transmission properties at the output ports of the device as a function of the height tolerance for two modes of Signal and LO and two switching states: (a–d) for TE_0 mode, and (e–h) for TE_1 mode.
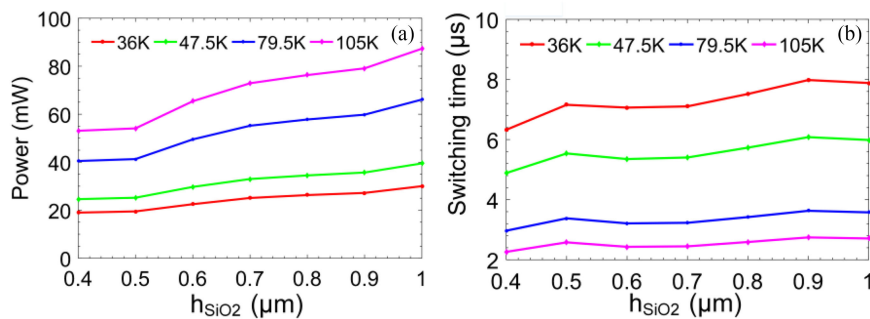

Fig. 11. Characteristics as a function of the gap between the metallic micro-heater and the silicon core layer: (a) power consumption, and (b) switching time.

Fig. 11 plots the required power to achieve a phase shift of π-radian P_π and the switching time τ for several different switching temperatures, measured by numerical simulation data, as functions to the gap of h_{SiO_2}. In general, simulated results show that the electric power consumption increases following the variable h_{SiO_2} for different switching required temperatures. At the designated gap of h_{SiO_2} = 700 nm, the levels of P_π are approximate to relatively small values of 25 mW, 32 mW, 55 mW, and 75 mW corresponding to different switching temperatures of 36 °K, 47.5 °K, 79.5 °K, and 105 °K, as seen in Fig. 11(a), respectively. Whereas, Fig. 11(b) shows that the sufficiently ultrafast

switching times are in turns of 2.5 μs, 3.2 μs, 5 μs, and 7.2 μs for determining the switching temperatures, respectively.

Finally, in comparison with related works proposed and demonstrated in several previous reports, such as related investigations in Ref. [18], [28], [30], our device has the same operating bandwidth as well as the same levels of optical performances. However, our proposed can be reconfigurable for optical line protection switch, and more importantly, it can be applied in an MDM-hybridized coherent optical communication system.

4. Conclusion

To summarize, we designed and optimized a 1 × 2 switchable dual-mode optical 90° hybrid device based on the SOI platform via different kinds of compact 2 × 2 MMI couplers, symmetric Y-junctions, and two metallic micro-heaters for controlling the switching states. The device exhibited an insertion loss lower than 2.5 dB, a common-mode rejection ratio better than −24 dB, an imbalance factor less than 1 dB, and a phase deviation smaller than 4° over 50-nm wavelength-bandwidth covered the C-band. The proposed hybrid coupler achieved width and height tolerances as much as ±50 nm, ±6 nm in 1.5 dB transmittance deviation. Besides, the proposed had a low power consumption under 75 mW, and an ultrafast switching time did not exceed 10-μs. This hybrid can be widely applied in various very-large-scale photonic integrated circuits, broadband optical phase modulators, and high-bitrate MDM-hybridized coherent optical communication systems because of its good performance and compact size.

References

[1] A. Sano, H. Masuda, T. Kobayashi, M. Fujiwara, K. Horikoshi, and E. Yoshida, "Transmission over 240 km using PDM-16-QAM modulation and digital coherent detection," in *Proc. Conf. Opt. Fiber Commun., Collocated Nat. Fiber Optic Engineers Conf.*, pp. 1–3, doi: 10.1364/NFOEC.2010.PDPB7.
[2] J. Yu, Z. Dong, H. Chien, Y. Shao, and N. Chi, "7-Tb/s (7 × 1.284 Tb/s/ch) signal transmission over 320 km using PDM-64QAM modulation," *Photon. Technol. Lett.*, vol. 24, no. 4, pp. 264–266, 2012.
[3] X. Zhou, "An improved feed-forward carrier recovery algorithm for coherent receivers with M-QAM modulation format," *IEEE Photon. Technol. Lett.*, vol. 22, no. 14, pp. 1051–1053, Jul. 2010.
[4] P. Dong, C. Xie, L. Chen, L. L. Buhl, and Y. K. Chen, "112-Gb/s monolithic PDM-QPSK modulator in silicon," in *Proc. Eur. Conf. Opt. Commun.*, 2012, pp. 624–629.
[5] Z. Li, "Compact low-loss opical 72° hybrid based on nonoverlapping-image multimode interference coupler in silicon-on-insulator," *IEEE Photon. J.*, vol. 11, no. 6, Dec. 2019, Art. no. 7907309.
[6] P. Dong, C. Xie, and L. L. Buhl, "Monolithic coherent receiver based on 120-degree optical hybrids on silicon," in *Proc. OFC*, 2014, pp. 1–3.
[7] M. G. Saber *et al.*, "Demonstration of a 120° hybrid based simplified coherent receiver on SOI for high speed PON applications," *Opt. Exp.*, vol. 26, no. 24, 2018, Art. no. 31222.
[8] M. G. Saber *et al.*, "25 and 50 Gb/s/λ PAM-4 transmission over 43 and 21 km using a simplified coherent receiver on SOI," *IEEE Photon. Technol. Lett.*, vol. 31, no. 10, pp. 799–802, May 2019.
[9] A. Melikyan, K. Kim, N. Fontaine, S. Chandrasekhar, Y.-K. Chen, and P. Dong, "Inter-polarization mixers for coherent detection of optical signals," *Opt. Exp.*, vol. 26, no. 14, 2018, Art. no. 18523.
[10] X. Xu, L. Shi, L. Ren, and X. Zhang, "Optical gradient forces in PT-symmetric coupled-waveguide structures," *Opt. Exp.*, vol. 26, no. 8, 2018, Art. no. 10220.
[11] B. Liu, X. Li, Y. Zhang, X. Xin, and J. Yu, "Probabilis shaping for ROF system with heterodyne coherent detection," *APL Photon.*, vol. 2, no. 5, 2017, Art. no. 056014.
[12] P. Kumar, S. K. Sharma, and S. Singla, "Performance analysis of an OSSB RoF link using 90° & 120° hybrid coupler," *Opt. Commun.*, vol. 373, pp. 114–118, 2015.
[13] K. N. Nguyen, T. Kise, J. M. Garcia, H. N. Poulsen, and D. J. Blumenthal, "All-Optical 2R regeneration of BPSK and QPSK data using a 90° optical hybrid and integrated SOA-MZI wavelength converter pairs," in *Proc. Opt. Fiber Commun. Conf. Exp., Nat. Fiber Optic Engineers Conf.*, 2011, pp. 1–3.
[14] C. R. Doerr *et al.*, "Monolithic demodulator for 40-Gb/s DQPSK using a star coupler," *J. Light. Technol.*, vol. 24, no. 1, pp. 171–174, 2006.
[15] L. Xu *et al.*, "Ultra-broadband and ultra-compact optical 90° hybrid based on 2×4 MMI coupler with subwavelength gratings on silicon-on-insulator," in *Proc. Opt. Fiber Commun. Conf.*, 2018, Paper M3I.7.
[16] O. Golani *et al.*, "A photonic analog-to-digital converter using phase modulation and self-coherent detection with spatial oversampling," *Opt. Exp.*, vol. 22, no. 10, 2014, Art. no. 12273.
[17] C. R. Doerr, L. Zhang, S. Chandrasekhar, and L. L. Buhl, "Monolithic DPSK receiver in InP with low polarization sensitivity," *IEEE Photon. Technol. Lett.*, vol. 19, no. 21, pp. 1765–1767, Nov. 2007.

[18] S. Jeong and K. Morito, "Compact optical 90° hybrid employing a tapered 2×4 MMI coupler serially connected by a 2×2 MMI coupler," *Opt. Exp.*, vol. 18, no. 5, pp. 4275–4288, 2010.
[19] L. Xiang, Y. Xu, Y. Yu, and X. Zhang, "An ultracompact DP-QPSK demodulator based on multimode interference and photonic crystals," *IEEE J. Light. Technol.*, vol. 30, no. 11, pp. 1595–1601, Jun. 2012.
[20] D. Kong, M. Tsubokawaa, and L. Chen, "A controllable nanosize combiner in T-shaped metal-insulator-metal waveguides," *IEICE Electron. Exp.*, vol. 13, no. 6, pp. 1–5, 2016.
[21] D. González-Andrade *et al.*, "Ultra-Broadband mode converter and multiplexer based on sub-wavelength structures," *IEEE Photon. J.*, vol. 10, no. 2, Apr. 2018, Art. no. 2201010.
[22] L. Xu *et al.*, "Broadband 1310/1550 nm wavelength demultiplexer based on a multimode interference coupler with tapered internal photonic crystal for the silicon-on-insulator platform," *Opt. Lett.*, vol. 44, no. 7, 2019, Art. no. 1770.
[23] P. Runge *et al.*, "Monolithic InP receiver chip with a 90° hybrid and 56GHz balanced photodiodes," in *Proc. OFC Opt. Fiber Conf.*, 2012, Paper OMT3.
[24] W. H. Liu, Y. L. Zhao, C. Z. Xu, J. Y. Zhao, W. Liu, and Y. Z. Xu, "Optical 90° hybrid based on an InP 4 × 4 multimode interference coupler for coherent receiver application," *Chin. Phys. Lett.*, vol. 29, no. 6, pp. 2011–2013, 2012.
[25] Y. Sakamaki, Y. Nasu, T. Hashimoto, K. Hattori, T. Saida, and H. Takahashi, "Reduction of phase-difference deviation in 90° optical hybrid over wide wavelength range," *IEICE Electron. Exp.*, vol. 7, no. 3, pp. 216–221, 2010.
[26] D. Hoffmann, H. Heidrich, G. Wenke, R. Langenhorst, and E. Dietrich, "Integrated optics eight-port 90° hybrid on LiNO$_3$," *J. Light. Technol.*, vol. 7, no. 5, pp. 794–798, 1989.
[27] L. Zimmermann, K. Voigt, G. Winzer, K. Petermann, and C. M. Weinert, "C -Band optical 90° -Hybrids based on Silicon-on-Insulator 4×4 waveguide couplers," *Photon. Technol. Lett.*, vol. 21, no. 3, pp. 143–145, 2009.
[28] K. Voigt, L. Zimmermann, G. Winzer, H. Tian, B. Tillack, and K. Petermann, "C-Band optical 90 hybrids in silicon nanowaveguide technology," *Photon. Technol. Lett.*, vol. 23, no. 23, pp. 1769–1771, 2011.
[29] W. Yang, M. Yin, Y. Li, X. Wang, and Z. Wang, "Ultra-compact optical 90° hybrid based on a wedge-shaped 2 × 4 MMI coupler and a 2 × 2 MMI coupler in silicon-on-insulator," *Opt. Exp.*, vol. 21, no. 23, pp. 1323–1331, 2013.
[30] H. Guan *et al.*, "Compact and low loss 90° optical hybrid on a silicon-on-insulator platform," *Opt. Exp.*, vol. 25, no. 23, 2017, Art. no. 28957.
[31] C. Sun, Y. Yu, G. Chen, and X. Zhang, "Ultra-compact bent multimode silicon waveguide with ultralow inter-mode crosstalk," *Opt. Lett.*, vol. 42, no. 15, 2017, Art. no. 3004.
[32] W. Bogaerts *et al.*, "Silicon-on-Insulator spectral filters fabricated with CMOS technology," *IEEE J. Sel. Top. Quantum Electron.*, vol. 16, no. 1, pp. 33–44, Jan./Feb. 2010.
[33] D. Ge *et al.*, "Experimental demonstration of ROADM functionalities for hybrid MDM-WDM optical networks," in *Proc. Opt. Fiber Commun. Conf. Exhib.*, 2016, pp. 1–3.
[34] Y. Tan and D. Dao, "Silicon-based hybrid demultiplexer for wavelength- and mode-division multiplexing," *Opt. Lett.*, vol. 43, no. 9, pp. 1962–1965, 2018.
[35] L.-W. Luo *et al.*, "WDM-compatible mode-division multiplexing on a silicon chip," *Nat. Commun.*, vol. 5, no. 3069, pp. 1–7, 2014.
[36] D. Soma *et al.*, "257-Tbit/s Weakly coupled 10-Mode c + L-Band WDM transmission," *J. Light. Technol.*, vol. 36, no. 6, pp. 1375–1381, 2018.
[37] H. Jia *et al.*, "WDM-compatible multimode optical switching system-on-chip," *Nanophotonics*, vol. 8, no. 5, pp. 889–898, 2019.
[38] L. Han, B. P. P. Kuo, N. Alic, and S. Radic, "Silicon photonic wavelength and mode selective switch for WDM-MDM networks," in *Proc. Opt. Fiber Commun. Conf. Exhib.*, pp. 1–3, doi: 10.1364/ofc.2019.m3b.4.
[39] P. Guo, W. Hou, L. Guo, Z. Ning, M. S. Obaidat, and W. Liu, "WDM-MDM silicon-based optical switching for data center networks," in *Proc. IEEE Int. Conf. Commun.*, 2019, pp. 1–6.
[40] H. Guan *et al.*, "Compact and low loss 90° optical hybrid on a silicon-on-insulator platform," *Opt. Exp.*, vol. 25, no. 23, 2017, Art. no. 28957.
[41] R. Ryf *et al.*, "Mode-division multiplexing over 96 km of few-mode fiber using coherent 6×6 MIMO processing," *J. Light. Technol.*, vol. 30, no. 4, pp. 521–531, 2012.
[42] T. Watanabe, B. I. Bitachon, J. Leuthold, B. Baeuerle, P. Ma, and Y. Fedoryshyn, "Coherent few mode demultiplexer realized as a 2D grating coupler array in silicon," *Opt. Exp.*, vol. 28, no. 24, pp. 36009–36019, 2020.
[43] L. B. Soldano and E. C. M. Pennings, "Optical multimode interference devices based on self-imaging: Principles and applications," *J. Light. Technol.*, vol. 13, no. 4, pp. 615–627, 1995.
[44] M. Uzma, M. Zaheer, A. Asif, and T. Azfar, "Effect of phase shifting on self-imaging in optical multimode interference devices," in *Proc. 2016 19th Int. Multi-Top. Conf.*, 2017, pp. 3–7.
[45] Á. Rosa, A. Gutiérrez, A. Brimont, A. Griol, and P. Sanchis, "High performace silicon 2x2 optical switch based on a thermo-optically tunable multimode interference coupler and efficient electrodes," *Opt. Exp.*, vol. 24, no. 1, pp. 191–198, 2016.
[46] M. Jacques, A. Samani, E. El-Fiky, D. Patel, Z. Xing, and D. V. Plant, "Optimization of thermo-optic phase-shifter design and mitigation of thermal crosstalk on the SOI platform," *Opt. Exp.*, vol. 27, no. 8, pp. 10456–10471, 2019.
[47] J. Parra, J. Hurtado, A. Griol, and P. Sanchis, "Ultra-low loss hybrid ITO/Si thermo-optic phase shifter with optimized power consumption," *Opt. Exp.*, vol. 28, no. 7, 2020, Art. no. 9393.
[48] N. C. Harris *et al.*, "Efficient, compact and low loss thermo-optic phase shifter in silicon," *Opt. Exp.*, vol. 22, no. 9, 2014, Art. no. 10487.
[49] V. M. N. Passaro, F. Magno, and A. V. Tsarev, "Investigation of thermo-optic effect and multi-reflector tunable filter/multiplexer in SOI waveguides," *Opt. Exp.*, vol. 13, no. 9, 2005, Art. no. 3429.
[50] K. Liu, C. Zhang, S. Mu, S. Wang, and V. J. Sorger, "Two-dimensional design and analysis of trench-coupler based silicon mach-zehnder thermo-optic switch," *Opt. Exp.*, vol. 24, no. 14, 2016, Art. no. 15845.